Title
Development of a multifunctional sediment consolidometer: Capable of concurrent measuring of bidirectional electrical effects, salinity, and fluid compositions

Author
Morgan-Witts, Natasha

Publication Date
2021

UNIVERSITY OF CALIFORNIA SAN DIEGO

Development of a multifunctional sediment consolidometer: Capable of concurrent measuring of bidirectional electrical effects, salinity, and fluid compositions

A thesis submitted in partial satisfaction for the
requirements for the degree of
Master of Science

in

Earth Sciences

by

Natasha Morgan-Witts

Committee in charge:

Professor Jeffrey Gee, Chair
Professor Yuri Fialko, Co-chair
Professor Emily Chin

2021

The Thesis of Natasha Morgan-Witts is approved, and it is acceptable in quality and form for publication on microfilm and electronically.

University of California San Diego

2021

TABLE OF CONTENTS

List of Figures

List of Tables

Acknowledgements

Chapter 1 and 2 are coauthored with Brown, Kevin. The thesis author was the primary author of these chapters.

ABSTRACT OF THE THESIS

Development of a multifunctional sediment consolidometer:
Capable of concurrent measuring of bidirectional electrical effects,
salinity, and fluid compositions

by

Natasha Morgan-Witts
Master of Science in Earth Sciences

The University of California San Diego, 2021

Professor Jeffrey Gee, Chair

We report here on the initial results from developing a prototype consolidometer focused on determining the anisotropic resistivity evolution in water-saturated sediments during burial. A key difference in this apparatus from comparable versions is the ability to simultaneously measure resistivity horizontally and vertically (parallel and perpendicular to σ_1 respectively), which allows for anisotropic effects to be determined. Complexities arise when clay fabrics generate anisotropic resistivity, along with two forms of total pore water (dual water). Dual water exists in consolidated high surface

area sediments, and is comprised of: (a) Electric Double Layer (EDL) attached to mineral surfaces, and (b) bulk pore water in the pore center. The EDL water is more saline and conductive than bulk water under pressure due to the density of counter ions required to balance the negative surface charge. Clays have comparatively large surface areas and EDL components compared to other sediments. As a result, clay-dominated sediments (a) have anomalously low resistance compared to low surface area granular sediments and (b) a net pore resistivity that should decrease during consolidation due to the preferential loss of low salinity bulk pore water and retention of the saline conductive EDL water.

The EDL increased salinity (reduced pore resistivity) effects should become acute at low porosities when the few tens of nanometer-thick EDL films become compressed (Brown et al., 2017) and are expected to partially counter the expected overall increases in resistivity with general porosity reduction. The anisotropy due to clay compaction fabrics is also expected to become simultaneously acute during compaction, addressing both effects concurrently is beneficial. Given this novel approach, this is a primarily technical report on developing a prototype consolidometer capable of simultaneously measuring porosity evolution and anisotropic resistivity, along with fluid composition and salinity. Future projects will address several associated themes related to consolidation, fluid flow, nanofilm interactions, and ultrafiltration responses in active tectonics and sedimentary environments.

This report also briefly describes the collection of over 270 hold-slip-hold trials on westerly granite. The data will be used in the future to build upon works like Brown et al. 2012 by incorporating a varied composition and fluid content(Mitchell et al., 2011, 2016;

Brown and Fialko, 2012). The main goals of this study are to continue work on wet melt mechanisms where fluid content effects were evaluated and incorporate clays into the mixture.

CHAPTER 1

1. INTRODUCTION

Water controls many significant structural and hydrologic processes at shallow to mid-crustal depths, including stress/depth vs. porosity trends, geopressures, fluid transport processes, and the general state of stress and fault dynamics in basins and plate boundaries. (Saffer and Bekins, 2006; Twiss and Moores, 2006; Diao and Espinosa-Marzal, 2018) We propose that porosity filled with bulk water almost ceases to exist with depth in phyllosilicate mineral-dominated systems globally(Brown and Ransom, 1996; Fitts and Brown, 1999; Neuzil and Provost, 2009; Brown et al., 2017). Here we define bulk water as the free water inside larger pores away from the electrostatic influences of charged mineral surfaces and their exchange cations (Neuzil and Provost, 2009; Mitchell, 1993). The change in water properties from bulk to EDL-dominated can significantly impact all the above structural and hydrologic processes. We start to address the strong linkages between the state of stress and various mechanical and chemical mechanisms of water release from sediments and resistivity trends during deep burial. At depth porosity evolution is particularly complex in high surface clay-bearing sedimentary sequences where mechanical consolidation, nanofilm confinement and ion dehydration, and thermally activated diagenetic reactions all play a role(Moore and Saffer, 2001; Brown et al., 2001, 2017; Saffer and Bekins, 2006; Saffer and Wallace, 2015)

The study presented here is a progression from past research done on nanofilms and EDL in high surface area sediments. It has direct relevance to the deeper hydrogeology of active tectonics and basin settings containing consolidating sediments and programs such as the Integrated Ocean Drilling Program (IODP) and Ocean Drilling Program (ODP) (Poeppe, 2016; Brown et al., 2017). The IODP and ODP have long studied the earth's surface, with an emphasis on oceanic basins. A notable series of studies for nanofilms have come from subduction zone settings such as the deep drilling IODP expedition 348, located at the Nankai Subduction System (Brown et al., 2017). We expect the resistivity effects described here to be significant at Nankai as well as most other subduction zones as there is an abundant illite and smectite component (40-60% total clay) and corresponding high surface area in the bulk sediment, leading to pronounced nanofilm effects(Brown et al., 2017).

The uniaxial consolidometer utilized in this study was substantially redesigned and produced by Dr. Brown as a significant modification from a prior titanium piston-cylinder design(Poeppe, 2016; Brown et al., 2017). The general geometry of the design structure came from an IODP Shipboard pore water squeezer. The IODP shipboard pore water squeezer was modeled after one developed by Manheim and Sayles (Sayles and Manheim, 1975). The prior designs of Dr. Brown, IODP, and Manheim and Sayles concentrated on tracking and collecting expelled pore water for chemical analysis. The version discussed here is substantially modified and essentially a new design focused on monitoring the anisotropic resistivity evolution of sediments under one-dimensional consolidation in addition to the compositional evolution of the pore water. The studies discussed here are particularly pertinent to the following hydrologic and geologic areas:

1. Permeability evolution in shales during burial.
2. Overpressure environments generated by the consolidation and release of fluid from bulk pores spaces.
3. Overpressure environments generated by the consolidation and stress-related release of fluids from the interlayer regions of hydrous clays such as smectite, kaolinite, montmorillonite, and vermiculite.
4. Over pressuring generated by thermal/chemical sources of water derived from hydrous clays such as smectite, kaolinite, montmorillonite, and vermiculite.
5. Estimates of porosity and over-pressuring based on the geophysical (i.e., electrical) properties of clays.
6. The evolution in the salinity and chemistry of pore fluids and the potential for osmotically derived fluid pressures, especially regarding argillaceous formations(Neuzil and Provost, 2009)
7. The ultrafiltration and evolution of isotopic compositions in pore water and solutes in response to consolidation and fluid flow.

1.1 Impacts of Consolidation on Anomalous Fluid Pressure

Fluid overpressures (above hydrostatic fluid pressures) are widely accepted as common causes of weak fault zones and hydrofracturing (Scuderi and Collettini, 2016; Koehn et al., 2020) in active tectonic settings. Over pressured environments are formed naturally through tectonics (due to rapid sediment burial and thermally activated dehydration reactions etc.). However, they can also occur through anthropogenic interactions (see table1.1).

Fluid overpressures (above hydrostatic fluid pressures) are widely accepted as common causes of weak fault zones and hydrofracturing Potential causes and sources of anomalous fluid pressure are listed in Table 1.1.

Table 1.1: Potential sources and causes of anomalous fluid pressure

Source	Examples
Tectonics	Rapid burial or erosion, areas of higher compression or stress
Structural Changes	Faults, ground collapse, often impacted by tectonics
Artesian Networks	Confined aquifers, changes in volume
Sediment Diagenesis	Interaction of water and rock/sediment is changed- ex cementation reduces permeability and porosity
Thermal Effects	Water expansion thermal gradients and frictional heating in earthquakes
Osmotically Generated	Chemical gradients
Biochemically Generated	Methane production
Anthropogenic Effects on Water	Pumping and building
Earthquakes	Stress and thermal changes
Chemical sources of water	Dehydration reactions in minerals and oil and gas generation

1.2 Background on nanofilms

In this study, nanofilms refer to the ultra-thin water films trapped between closely spaced (<a few 10's nm) charged mineral surfaces that form in response to electronegative clay surfaces interacting with the bulk pore water to form an electric double layer (EDL). The surface charge density of mineral (γ_e) can be taken from the literature with ranges generally between around 0.75-1.5 charges per nm^2 surface area (Kaufhold et al., 2011; Holmboe and Bourg, 2014; Guo et al., 2017). The negative surface charges are balanced by counter ions that become hydrated to form the EDL. Surface charge densities can be determined from the cation exchange capacities (C_{ec}, cmol/1000g sediment) of sediments as-long-as the surface area (a_s in m^2/g) is also known such that:

$$\gamma_e = \frac{C_{ec} A_v}{a_s . 10^{23}} = \frac{6.022 C_{ec}}{a_s .}, \qquad (1)$$

where A_v is Avogadro's number (A_v = 6.022*10^{23}). Typical C_{ec} values range between 100-200 cmol/1000g for smectite and 10-50 cmol/1000g for kaolinite. Clay-dominated sedimentary systems such as sedimentary basins and subduction faults (Underwood and Kubo, 2013; Schleicher et al., 2015) have abundant clay minerals with large smooth contacts (Fig. 1.1) and very high surface areas (a_s). Examples include various hydrous smectites and vermiculites (respectively A_s = 800 and 500 m^2/g), illite (40-175 m^2/g), kaolinite (10-45 m^2/g) (see Cerato and Lutenegger, 2002; Kellomaki, et al.,1987; Mitchell, 1993; Neuzil and Provost, 2009). In such systems, the EDL component of the dual pore water becomes increasingly dominant as the bulk pore water component is expelled during consolidation. The EDL thickness varies with salinity; however, at a few

10’s nm, thicknesses can have local concentrations equivalent to several Molar equivalents(Brown et al., 2001). This can be compared to typically~0.5-0.6 M or less in the bulk pores in seawater settings.

Nanofilms are generally present within the interlayer of hydrous clays such as smectites, but can also form at low porosities in any tightly confined pore with a strong prevalence of high surface area clay-dominated sediments. The basic structure of these nanofilms is shown in figure 1.1. The Stern model, pictured in figure 1.1, was developed from the Gouy-Chapman model. The Gouy-Chapman model described how electric potential exponentially decreased when away from the electronegative surface (in their case, metals). With the Stern model, assuming the mineral is suspended in bulk pore fluids, the layer closest to the electronegatively charged particle is termed the Stern layer (Butt et al.) The slipping layer consists of more loosely oriented and attached ions and hydrating water in a broader layer external of the Stern layer. (Park and Seo, 2011; Butt et al.)

The EDL structure consists of both the Stern and slipping layer. The slipping layer forms as a response to the electro-positivity of the Stern layer; however, it is not as concentrated due to the exponential decrease of electro potential away from the charged particle. The slipping layer thickness greatly expands at low pore water salinities to several 10’s nm(Favaro et al., 2016). The diffusive or bulk water region lies beyond the Stern and slipping layers. With the distance away from the negatively charged particle, there is little to no attractive or repulsive forces felt from the particle. Thus, there is no distinct order to the charges in the bulk pore fluids (see figure 1.1)

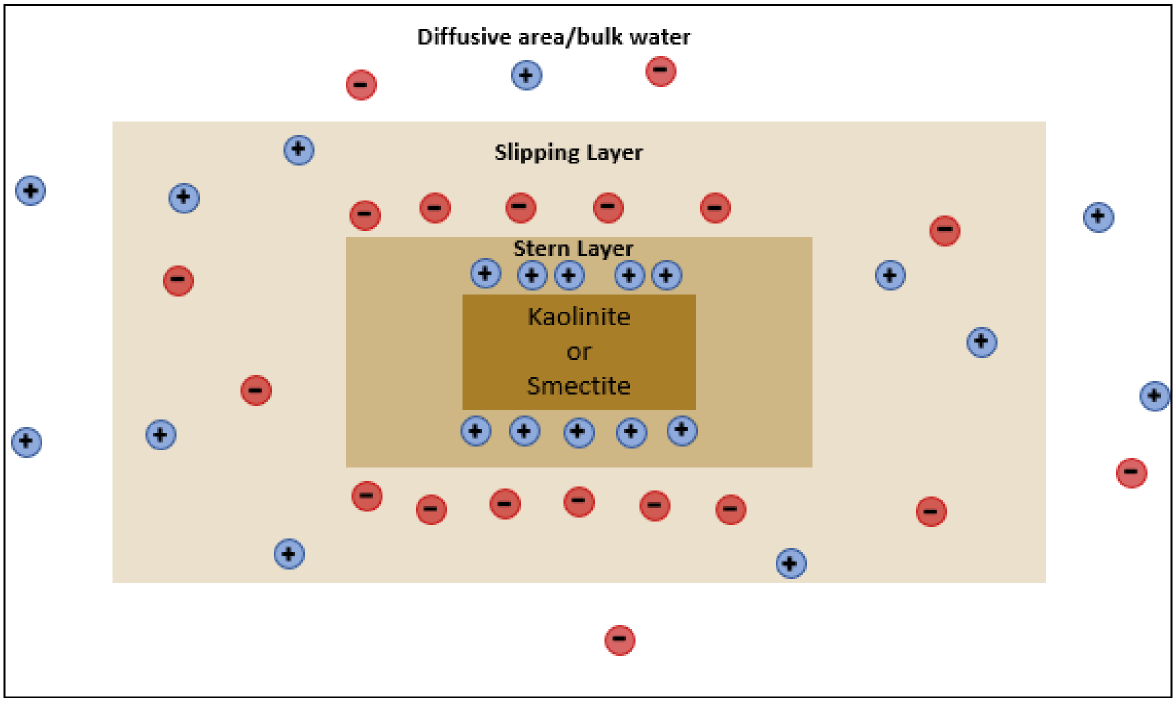

Figure 1.1: A basic schematic of a single tabular clay particle interaction with anions and cations present in bulk saline water. The stern layer is the closest to the electronegative outside of the clay particle, the slipping layer follows the stern layer with a lower concentration of ions.

During consolidation, the EDL properties become increasingly significant as proportionally more bulk pore fluids are expelled. During compaction, the lower salinity bulk pore fluids are preferentially reduced, increasing the net salinity and thus conductivity of the tightly bound saline EDL-dominated surface films. Figure 1.2 shows the pore evolution of a loosely to a more well-compacted clay sample. In an ideal sample, the initial environment has space for bulk water, lower salinity areas, and no charge pattern in the bulk pore water area

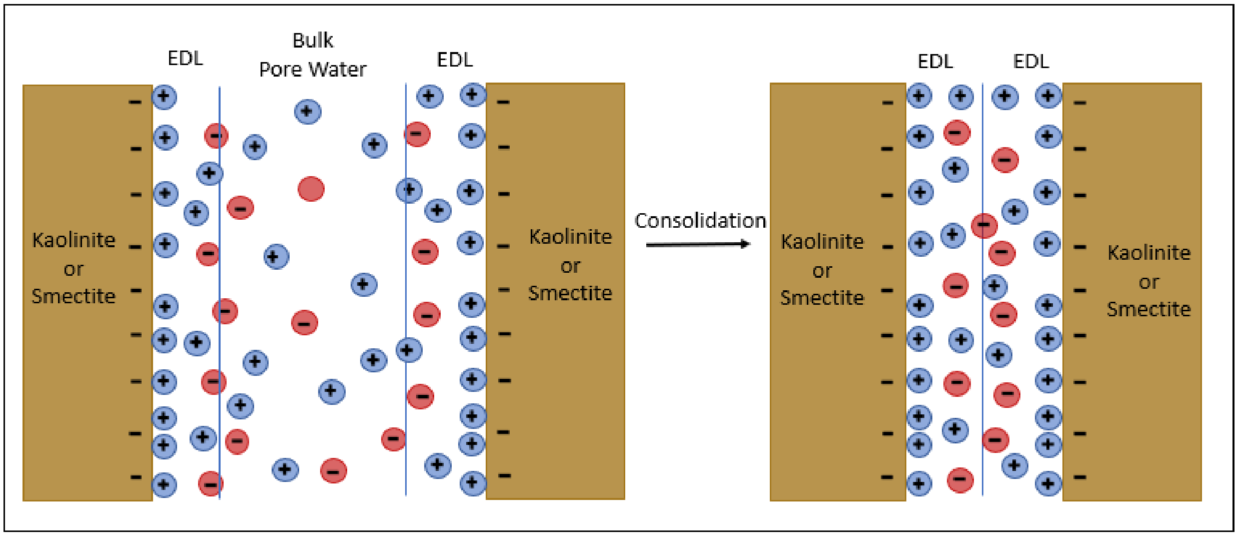

Figure 1.2: General schematic of the evolution of EDL and bulk water areas during compaction. The bulk pore fluids typically have a considerably lower salinity even in seawater than the EDL layer (which can be several M). Thus, as the bulk pore fluids are expelled during consolidation the net residual pore salinity increases and the thin film resistivity falls (i.e. conductivity increases). The effect is particularly noticeable in high surface area clay-rich formation but highly subdued in low surface area formations such as clean sandstones (<<1m^2/g). Even amongst clays low surface area Kaolinite (24 m^2/g) are expected to show less impact of the EDL than high surface area illite (105 m^2/g) and extremely high surface area hydrous smectites (surface area look up ~700-900 m2/g) (Kahr and Madsen, 1995).

pattern in the bulk pore water area. Post significant consolidation, the bulk pore water area has been compressed out of the environment, and the EDL dominates. The electronegative charges formerly on each side of the slipping layer are now being compressed into one more cohesive layer or out of the environment. See the theoretical evolution of this environment in figure 1.2.

1.3 Anisotropy and Dual Water

Changes in travel path length or tortuosity in sediments affect various transport mechanisms such as ionic transport, hydraulic conductivity, and resistivity. Generally, tortuosity increases as porosity decreases and direct flow paths become reduced. The electrical tortuosity, τ_c, is generally defined as;

$$\tau_c = \left(\frac{L_c}{L_o}\right)^2 \qquad (1)$$

Where L_c is the tortuous current path length and L_o is the direct path length across the sample(Abderrahmene et al., 2017). The electrical tortuosity is dependent on both porosity and sediment mineralogy (shape fabrics). For an isotropic granular material (e.g., clean sand/silt) with a low surface area, τ_c can be inferred from the electrical resistivity of a media as a simple product of its porosity (ϕ) and Formation factor (F) (Abderrahmene et al., 2017):

$$\tau_c = F\phi = \frac{R_f}{R_w}\phi \qquad (2)$$

There should be little variation in τ_c with respect to orientation for clean isotropic granular materials (round grains) undergoing vertical one-dimensional consolidation. Typically we expect tortuosity values in all orientations to remain low to moderate (values between 1-4) in clean sands. (Abderrahmene et al., 2017)

The value of τ_c can, however, be heavily influenced by the preferred orientation and surface properties of any tabular high surface area minerals or open fractures. Under compaction, kaolinite (and other clay minerals with a similar platy structure) will progressively orient perpendicular to the direction of σ_1. This orientation creates a discrepancy between the anisotropy in the vertical direction (σ_1) and the horizontal direction perpendicular to σ_1. An anisotropic tortuosity (figure 1.3) distribution develops with consolidation because (1) the low conductivity of the sheet silicate structure increasingly impedes vertical current flow perpendicular to the clay alignment, while (2) the preferred horizontal orientations of the sheet-like clays and attached conductive EDL layers will assist horizontal current flow (Fig. 1.3). As illustrated in figure 1.3, the vertical tortuosity should, thus, increase at a greater rate than the horizontal tortuosity as porosity is reduced. This tortuosity variation will manifest as increasing anisotropy in resistivity in the horizontal R_h and vertical R_v directions, with $R_v \gg R_h$ as porosity reduces.

The relationship between porosity and resistivity can be shown through Archie's Law and subsequent derivations, assuming conductivity in the system comes from pore water, and the sediment and silicates (clays) are essentially nonconductive. A form of Archie's law specifically for dual water in clays is the Waxman-Smits model, which has also been adapted for various environments. All adaptations of the Waxman-Smits model incorporate conductivity and cation exchange capacity terms and are well suited for the environments investigated in this research. A further discussion of Archie's law and the Waxman-Smits model is presented in appendix A.

The kaolinite we use in this study has a small "brick-like" aspect ratio and modest surface area and should produce only a modest anisotropic resistivity departure in response to compaction. However, we expect to get considerably more anisotropy in resistivity developing in high surface area and high aspect ratio clays such as smectites as they have thin sheet-like geometries. Smectite samples will be reported in future literature, as they were not completed due to time constraints.

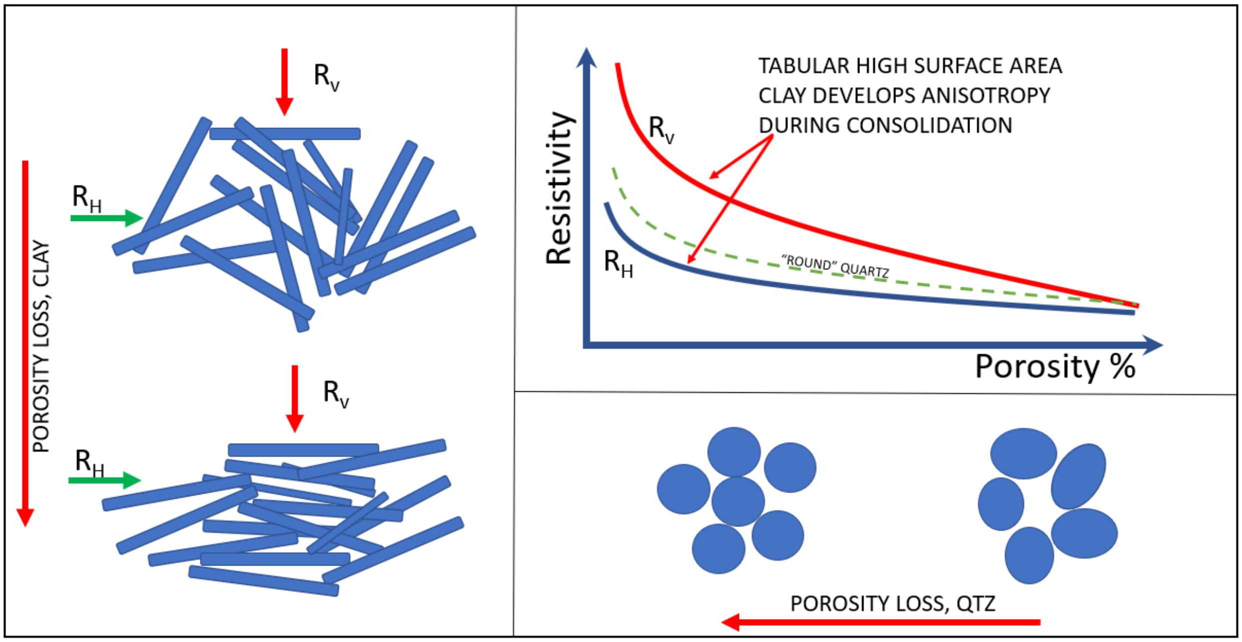

Figure 1.3: Schematic representation of the anisotropic alignment of tabular (A) clays and attached conductive EDL layers vs. the more isotropic packing of (B) quartz during consolidati and porosity loss. The fabric and alignment effects should result in a related marked anisotrop in (C). Resistivity/conductivity of the clay dominated samples vs a nearly isotropic response in sands.

1.4 Experiment Construction

The piston-cylinder consolidometer discussed here allows simultaneous consolidation, anisotropic resistivity measurements, and fluid composition measurements. To accomplish this combination of measurements, we electrically insulated the consolidating sample while allowing for one-dimensional consolidation. In addition, due to the lack of strength of many nonconductive insulators, we developed a new composite design where the nonconductive elements are enclosed within a strong ridged outer metallic sheath that could withstand elevated stresses imposed on the samples.

The resulting prototype consolidometer chamber has two key layers, (1) an aluminum outer cylinder, piston, and base plate, and (2) a highly nonconductive resin-filled fiber composite inner shell, baseplate cover, and Teflon piston that are in direct contact with the sample. Because the inner insulating composite is not highly scratch resistant, the moving inner piston was changed from an aluminum piston to one composed of Teflon which offers significantly lower friction against the fiberglass composite. O-rings on the piston were employed to contain the sample and pore fluids, which were expelled into sample vials through a 1.5 µm pore size porous filter inserted into the moving internal Teflon piston. The Teflon piston expands a small amount laterally at high pressures, increasing seal efficiency. The tests described here were conducted at low internal fluid pressures and will be increased as more trials are conducted. No leakage of pore fluids was detected even at high stresses. The sample chamber is capped at the bottom with a nonconductive layer that holds the lower sensors. The lower end cap is sealed onto the cylinder with O-rings, sealant, and is compressed onto the chamber when the upper and lower frame pieces and bolts. (see figure 1.5)

Two aluminum sheets are used as the upper and lower frame and are held together with four bolts. These frame plates are not load-bearing and are used to hold the different components of the apparatus together. Above the internal Teflon piston, there is a short aluminum piston with space for the electrode wires to exit the cylinder without being compressed. This piece is slightly smaller than the width of the sample chamber and is centrally placed so it does not scratch the fiberglass cylinder coating. (see figures 1.4 and 1.5)

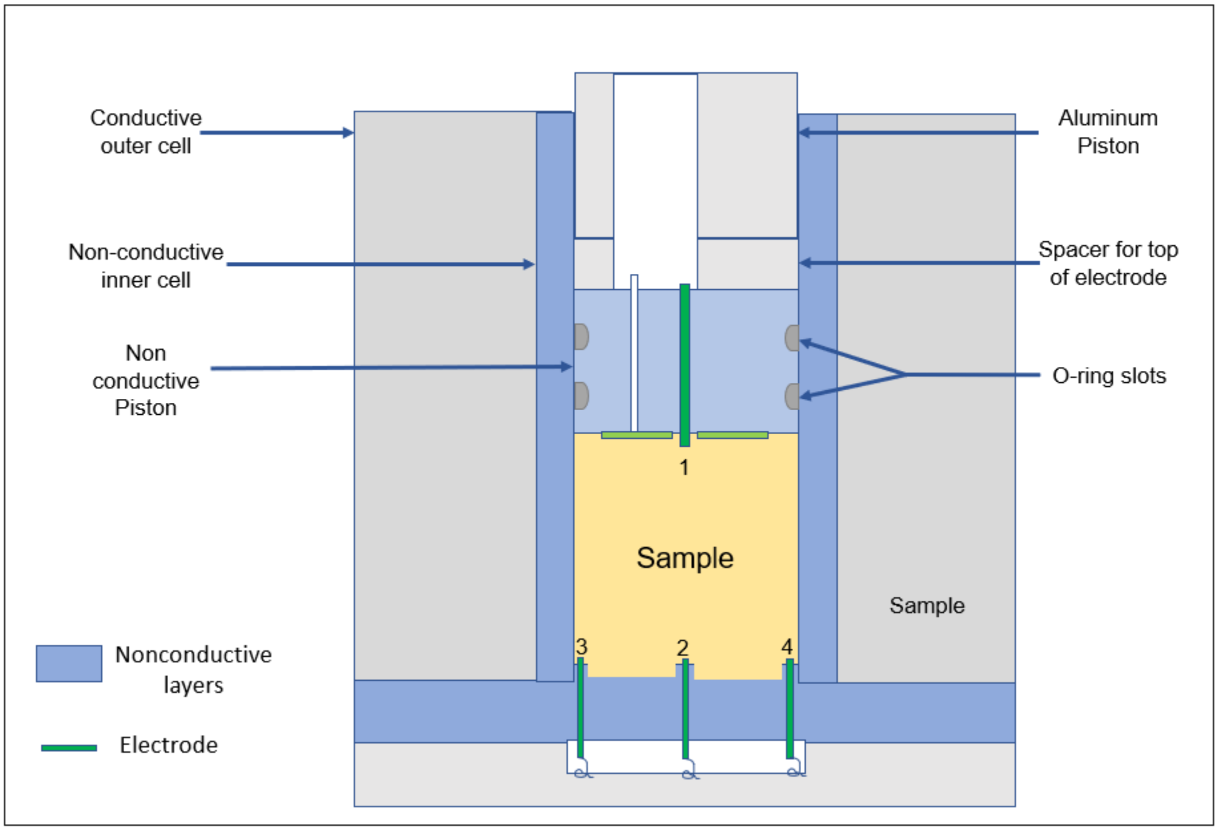

Figure 1.4: General schematic of the consolidometer structure and layers.

The sensor plate contains three detectors/electrodes in line with 1.35 cm between each. The outer electrodes are 0.1cm away from the cylinder walls. The electrodes are identical and are 0.64 cm in diameter and protrude 0.25 cm above the sensor plate. The base of the sensor plate has a gap for wiring to prevent them from being crushed during compression (see figure 1.4).

The consolidometer structure is in an ENERPAC load frame rated to 50 Tons. The load frame is rigged to a hydraulic system and controlled by a Teledyne ISCO Series D pump (see figure 1.5). The amount of compression was recorded directly using a Silverline high precision 50 mm dial indicator (0.01mm accuracy) and regulated with a direct measurement from the top of the consolidometer chamber to a marked area on the load piston as a secondary backup measurement.

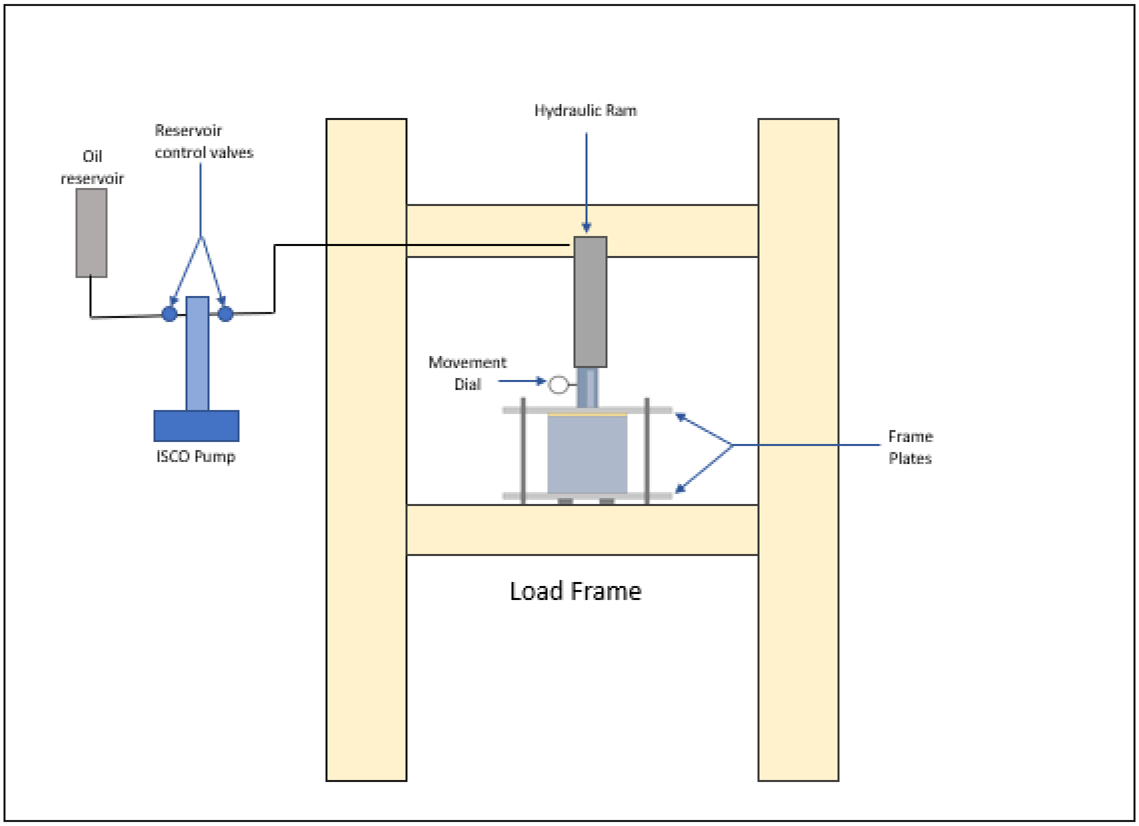

Figure 1.5: Overall schematic of the consolidometer structure and hydraulic structure. The high precision ISCO pump and oil reservoir are used to load the sample either in a load-step-load fashion or via a defined segment of constant displacement rate to a predefined strain increment. Displacement was constantly monitored to allow the porosity of the sample to be back-calculated from the final water content measurement.

1.5 Sample Preparation

Kaolinite samples were acquired in a pre-ground form from Wards Science (Lot No. 438590). The quartz sample came from pure vein quartz and was provided in a pure-crystal form (See figure 1.6, A). The quartz was manually ground to a maximum size of 0.104 mm before the following sample preparation steps(figure 1.6, B).

The samples went through three phases of mixing with seawater, settling, and excess seawater removal. The purpose of this was to ensure that seawater was well incorporated into the sample. The samples were then centrifuged and separated from excess water to reduce the saturation and deposited into the sample chamber. A small sample of the wet mixture was removed, weighed, and dried to conduct an initial porosity evaluation. An initial consolidation phase prior to measurements allowed for air removal seating of the seals around the piston. Typically, minimal loads were applied during this initial phase as the water contents were highly elevated.

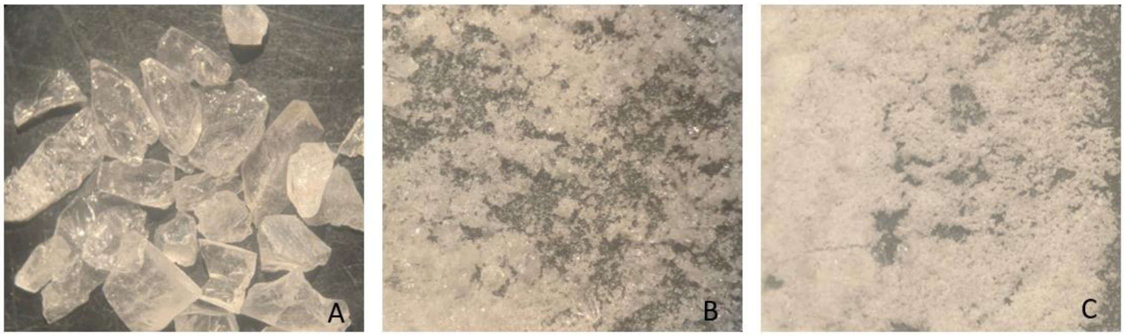

Figure 1.6: (A) pure vein quartz (B) ground pure vein quartz (C) post consolidation experiment-pure vein quartz and evaporates from seawater.

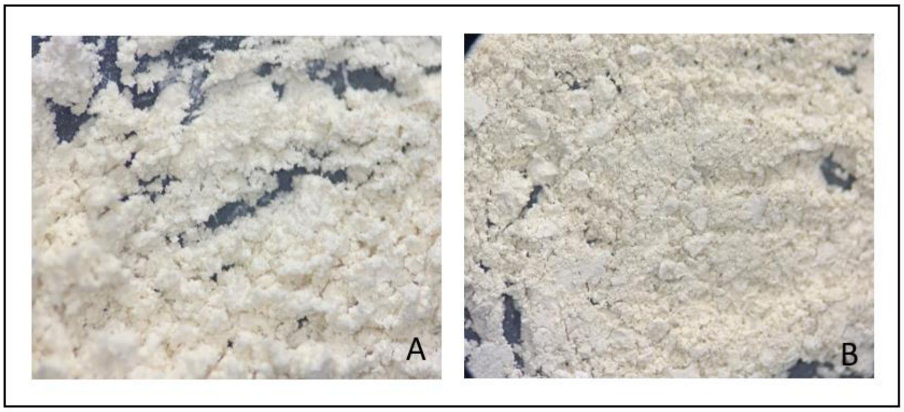

Figure 1.7: (A) Unaltered kaolinite sample directly from the supplier (Wards). (B) Kaolinite post consolidation experiment- pure kaolinite and evaporates from seawater.

1.6 Simultaneous measurements of porosity, load, fluid composition, and anisotropic resistivity.

The consolidation chamber geometry utilized for these experiments is modified from the ones used in (Poeppe, 2016; Brown et al., 2017). As described above, the major changes to the basic piston-cylinder configuration were the addition of (1) a fiberglass insulating barrier around the sample and (2) electrodes to the bottom of the sample chamber and into the moving upper Teflon piston (figure 1.4). The four electrodes were connected to a switch box that allowed different pairs of sensors to be put into the Wien's bridge measurement circuit (figure 1.8). For example, connecting electrodes 1 and 2 allowed the vertical resistivity to be measured perpendicular to any layered fabric developed in consolidating clays (figure 1.4). Connecting 2 to 3 or 4 to 3 allowed the horizontal resistivity to measured parallel to the aligned clays (figure 1.4). In addition, an Elenco Model RS-500 Resistance Substitution Box was placed in series with the sample to provide a further known internal calibration when processing the data (See figure 1.8 and Calibration section).

The resistance measurement circuit we constructed consists of the following main elements (figure 1.8)

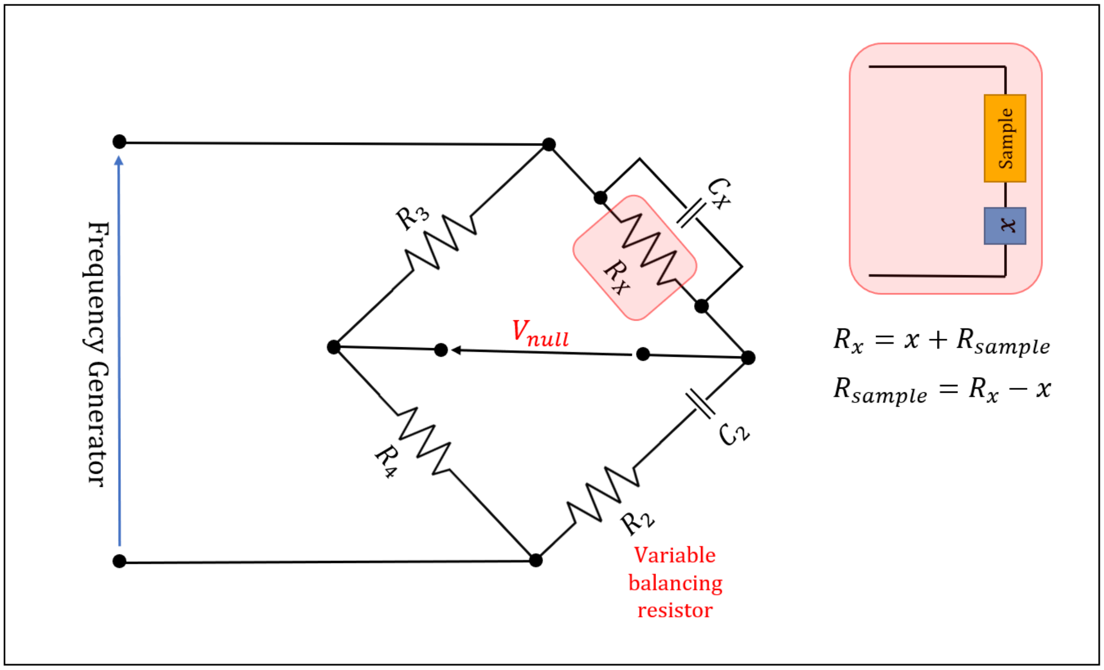

Figure 1.8: Wien's bridge and measurement system schematic. R_x and C_x are the samples resistivity and capacitance. The values for the Wiens Bridge Circuit are as follows R_3 = 1468 Ω , R_4 = 470 Ω, and C_2= 0.1 µF. The values of R_2 is determined by balancing the bridge to generate a zero Vnull value using the R_2 variable balancing resistor (an Elenco Model RS-500 Resistance Substitution Box).

1) Frequency generator (Koolertron DDS Signal Generator/Counter)
2) An Elenco Model RS-500 Resistance Substitution Box (X in figure 1.8) as a standard in series in with the sample.
3) The Wien's Bridge (Figure 1.8) is composed of known resistance and capacitance standards and an Elenco Model RS-500 Resistance box used as a variable balancing Resistor (R_2) capable of values from 1 Ω – 11 M-Ω in one-Ω steps.

4) The Null Voltage detector (V_{null}) was a PC-based high-frequency data acquisition system that precisely measured using a filtered Voltage signal across the bridge. The bridge is balanced when V_{null} equals zero.

5) Switch box allowing for us to balance the circuit, thus finding R_2. The R_2 values are later used to solve for R_x.

6) A sinusoidal waveform was applied from a Koolertron DSS Signal Generator/Counter, the frequency of which is changed from 1-7 MHz(±0.01Hz) throughout the experiment.

1.7 Theory/Calculations

Max Wien developed the Wien's bridge in 1891 to measure unknown capacitances and resistances in oscillating circuits by comparing them to know standard values. Its initial usage was mostly for frequency determination; however, the uses and adaptations of this method have significantly grown over time. The Wien bridge construction discussed here is now commonly used for resistance and capacitance determinations. Adaptations of the Wien bridge may include inductors, low and high pass filters, more resistors and conductors, and more depending on the intended purpose.

The switch box and sample sensors discussed in section 1.6 were wired into a Wien's bridge construction (see figure 1.8). At some frequency, the reactance of the R_2-C_2 arm will be an exact multiple of the shunt or sample arm (R_x-C_x) depending on the R_3 to R_4 ratio. For our measurements, we step the oscillation frequency utilizing the frequency generator between 1- 7 MHz. We then balance the bridge by varying R_2 so that the measured V_{null} falls to zero. When the bridge is balanced, the following two equations apply:

$$\omega^2 = \frac{1}{R_x R_2 C_x C_2} \qquad (1)$$

$$C_x = C_2 \left(\frac{R_4}{R_3} - \frac{R_2}{R_x}\right) \qquad (2)$$

These can then solved simultaneously to obtain R_x by substituting for C_x :

$$R_x = (\frac{1}{R_2\omega^2C_2^2})\frac{R_3}{R_4} \qquad (3)$$

Thus, when the bridge balances and V_{null} is zero, we substitute the known values of R_2 (determined from an Elenco Resistance Box by balancing the circuit), R_3, $R_{4,}$ and C_2 into Eqn. 3 to obtain R_x at any defined measurement frequency and for a predefined X (figure 1.8)

1.8 Results

Calibration

We include the calibration sections as a part of the results as this is a prototype design and method, and calibrations are a fundamental part of the method. With developing this prototype system, a considerable amount of time was taken to conduct calibrations and consistency tests to determine the precision and longevity of the system, as a test can take multiple weeks. Quality assurance tests were performed numerous times over weeklong periods to ensure consistent and representative results of the testing material over long timescales given potential issues such as seawater corrosion. Long-term data quality tests also found some impact from stray voltage between wires and wire to load frame. The laboratory was also found to be quite electromagnetically noisy. It took several weeks to properly isolate the load frame, sample, and wires connecting the sample to the Wien's bridge from electrical interference. For instance, removing many outside power sources and electronic sensors from the load frame significantly decreased scatter in the data.

Other extraneous sources of electrical disturbance primarily arose from potentials generated from individual contacts and, most importantly, from corrosion of the connections between the electrodes and the measurement wires. Issues arose if any water escaped during the initial compaction step because it created secondary corrosion effects and short circuits on the top vertical sensor in the movable Teflon piston. Multiple electrode connection structures were tested before a stable zero voltage across a sea water-filled cell utilizing the Wien's bridge succeeded. Eventually, a combination of a flexible silicone sealant and a water-resistant electrical tape provided enough insulation to avoid short circuits on the vertical sensor even when water was present near the contact.

The movement dial was improved throughout the trials, specifically through its mounting structure and stability beneath the sensing pin. One refinement came from improving the mounting structure of the dial to the system to make it less sensitive to non-hydraulic movements, such as the frame being touched. Subsequently, the stand the dial sensing pin rests on was changed to a sturdier structure to prevent non-hydraulically sourced movements.

Typically, the Wien's bridge measured the combined resistance (R_x) of the sample (R_{sample}) plus the calibration standard (X). The standard was stepped between 100 and 600 Ω at each chosen frequency, and the bridge balanced to obtain R_x. The resulting data could be plotted against the known resistance expected for a seawater-filled system (no sample) to calibrate the system for both electrode geometry and any residual frequency effects.

It was found that there were both frequency and electrode geometry effects present in the apparatus. Some frequency effects were expected due to the high sensitivity of the Wien's bridge construction to frequency and sinusoidal wave distortions from an applied voltage (e.g., the sinusoidal wave may not be perfect). Geometry effects present were multifaceted- the electrodes were relatively small, and the distance between electrodes in the vertical direction was constantly moving. To remedy this, standard seawater was taken to create a calibration curve at the same $R_{standard}$ and frequency as the sediment samples. This seawater curve was subsequently scaled to a standard seawater value of 0.2 Ω/m. This scaling factor step corrected the found seawater data and increased the relative size of found resistivity values, which aided in the future analysis since the resistivity values are very small.

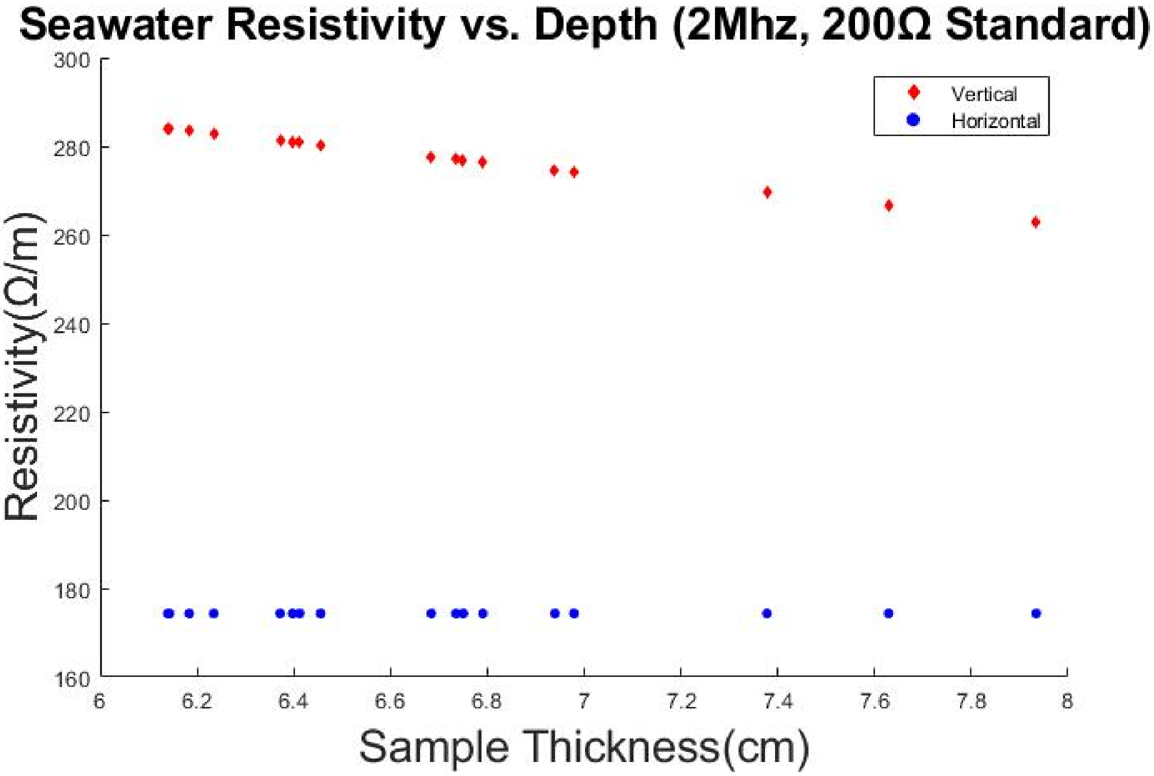

Figure 1.9: The vertical seawater evolution(blue) and horizontal evolution (orange), are consistent. As expected, the horizontal data from the seawater calibrations (perpendicular to σ_1) was relatively consistent at all depths, thus it was averaged. The vertical data shows a linear upwards trend consistent with piston movement. We expected resistance to decrease with depth, as there would be less seawater between sensor 1 and 2. This was not observed here, however the data was still used for calibration as the errors are systematic and very likely present in the sediment trials.

Multiple calibrations were incorporated after data collection to correct electrode geometry and sample effects. Through initial quality checks, it was determined that calibration was needed for the Elenco Model rS-500 substitution boxes. In theory, the boxes should read equivalent values; however, when connected with no sample or system involved there was a slope difference and offset between the boxes. The datasets were not specifically corrected for the box-box calibrations, as the box-box effect is included in the seawater data and removed once the seawater effect is removed. Although the box-box slope was not individually corrected, it is reported here to show an area of improvement for future trials.

The next phase of calibrations was to adjust for the vertical distance effect. As discussed in section 1.7, a horizontal and vertical measurement was taken, as the sample compresses the vertical sensors approach each other and show distance effects not present in the horizontal dataset. Calibration for the distance effect was done by comparing horizontal and vertical measurements of seawater at different depths in the sample chamber. From this, we can extrapolate the distance effect and adjust for vertical datasets(see figure 1.9 for seawater calibration). This calibration was not done through all datasets, as the vertical data was limited in some trials due to short circuits or system issues(see section 1.9 for more detail).

As seen in fig 1.9, the horizontal seawater data showed no significant changes or slope as the sample was reduced. As such, the experimentally derived seawater values were averaged and then equivalently scaled to the 0.2Ωm standard.

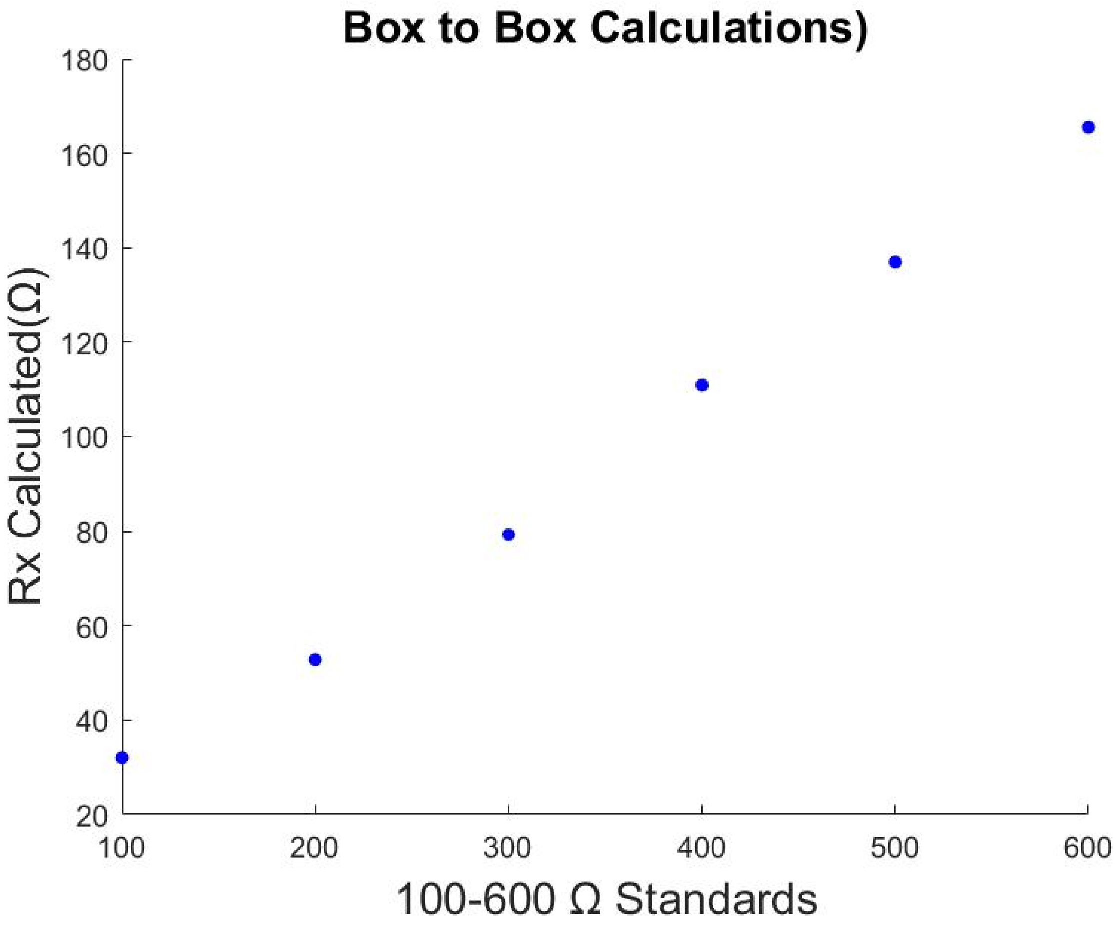

Figure 1.10: Box to box calibration of Elenco Model rS-500 Substitution boxes. The R^2 value shown here is 0.994.

The resistivity effects of pure seawater were also incorporated into the calibrations, as the focus of the study is on the clay/quartz EDL impacts rather than the impact of free-floating seawater. Once the resistivity effects were removed from the dataset, the remaining resistivity values were significantly scaled-down.

Sample Results

The quality of data produced throughout the development of this prototype consolidometer has consistently increased throughout the trials. The most recent sample data is the quartz, which is focused on here as it is the best indicator of the status of the consolidometer design and function. Earlier trials including the Kaolinite sample were subject to corrosion issues, short circuits, stray voltage issues, and more. Sources of error were improved through trials, however, are not fully remedied.

The general form of the data is close to the expected trends, with progressively increasing resistivities as the sample consolidates and porosities are reduced. For both kaolinite and quartz, we expected an upwards trend in the horizontal measurements. For the vertical measurements, we expected a slow upwards trend then near exponential change from kaolinite, and a slow upwards trend from the quartz. The trends look smooth and consistent along trend, and we do not see any sudden offsets or problems with balancing the Wien's bridge that can occur with the onset of stray potentials or significant corrosion.

A significant error in the Kaolinite trial came from the vertical sensor failing mid-trial, likely due to a short circuit or accidental compression or kinking of wires. It was found that the connector for sensor 1(figure 1.4), located on the top of the Teflon piston, was sensitive to corrosion and was easily kinked. To fix this sensor, the sample would have had to been unloaded and removed, which would invalidate the consistency of the trial. With this said, we continued to collect the horizontal data until a power cut initiated automatic de-pressurization of the system. Through seawater trials (no sediment) it was found that even small traces of seawater can cause the sensor to fail. Additionally, there

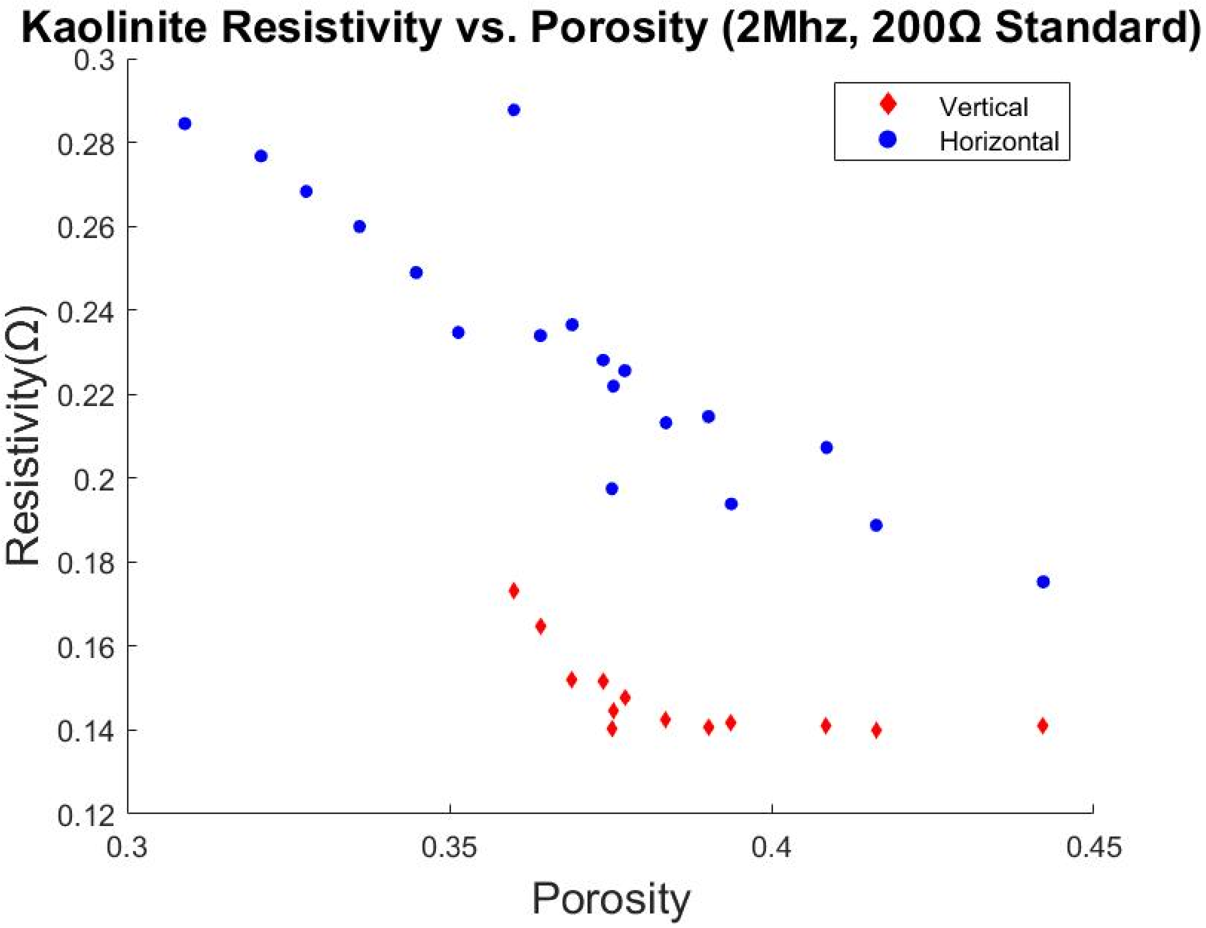

Figure 1.11: Kaolinite resistivity (Ω/m) vs. porosity. Horizontal data is perpendicular to σ_1 and shows a consistent upwards trend with a linear R^2 of 0.8011. Vertical data (σ_1) has a much more subtle upwards trend in the beginning, then changes to a near exponential evolution. The second order polynomial R^2 is 0.7222.

is a possibility that moisture in the air alone may cause corrosion over time, eventually causing the detector to fail. The wiring from sensor 1 is relatively enclosed, as it must pass through an aluminum spacer and the aluminum piston to reach the circuit. The possible corrosion issue is not apparent on the lower detectors (2-4, figure 1.4) that lead to open air. Impacts from corrosion would likely build over time, which would lead to a consistently propagating error. This error was noticed during the Kaolinite trials, where sensor 1(figure 1.4) failed mid-trial. As such, the data produced during the kaolinite trials should be interpreted with caution.

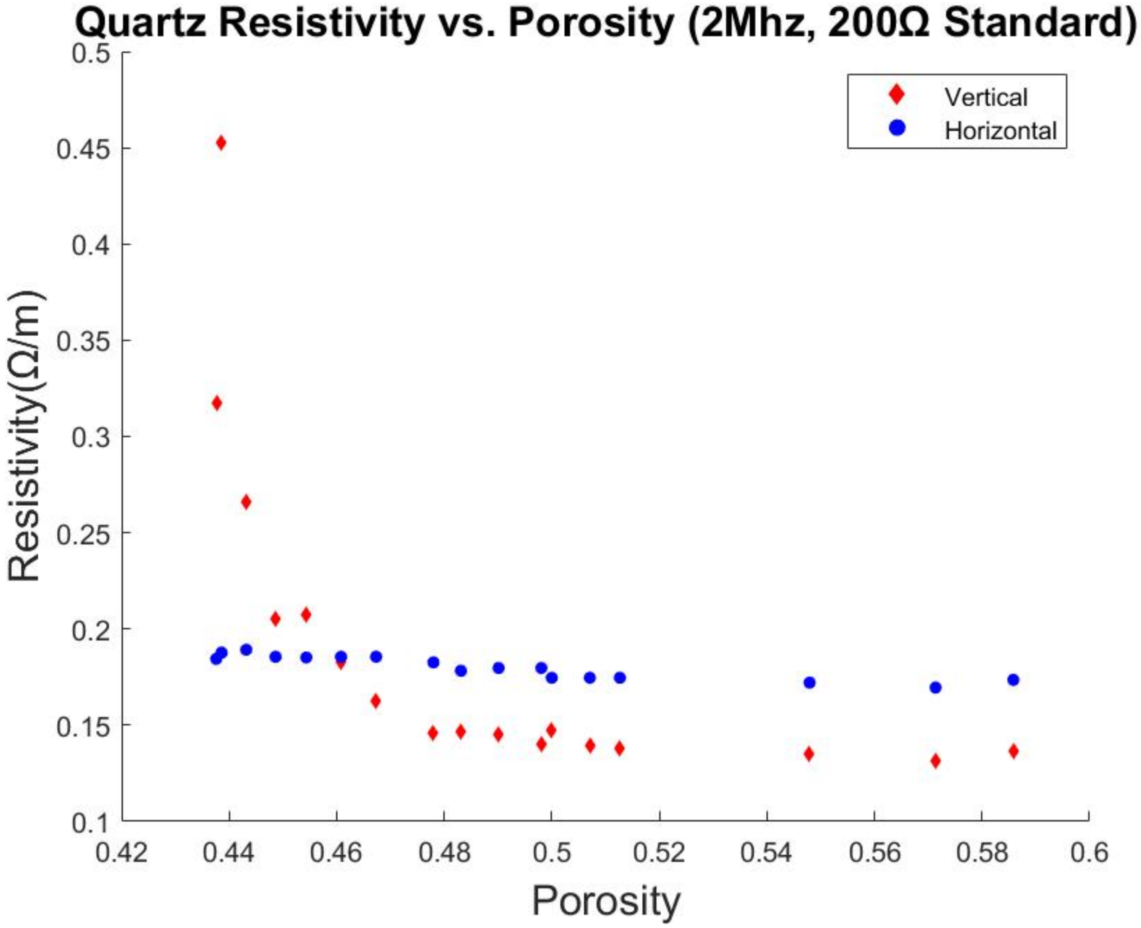

Figure 1.12: Quartz resistivity (Ω/m) vs. porosity. Horizontal data is perpendicular to σ_1 and shows a slow yet steady upwards trend with a linear R^2 of 0.828. Vertical data (σ_1) has a similarly subtle upwards trend in the beginning, then changes to a near exponential evolution. The second order polynomial R^2 0.7101.

The quartz trial had a much higher longevity compared to the kaolinite, and shows less scatter. Both horizontal and vertical data show an upwards trend, with the resistivity change in the vertical being the most significant. The significant difference between the two quartz series indicates a possible error within the consolidometer (further discussed in section 1.9)

1.9 Discussion

As this study is primarily on the development of a prototype consolidometer, the focus was on incrementally evolving the experimental method, physical system, and strategy. The calibrated data shows that the system can produce results that match with the expected, and is a good indicator of good futures results (see section 1.8). Results from the final quartz trial are very encouraging and point to the possibility of addressing the major scientific theme discussed at the start of this thesis. For example, as expected, the initial horizontal and vertical resistivities are very similar at high porosities. They are scaled to the same seawater ratio and evolve along reasonable-looking trajectories during subsequent consolidation. However, some potential improvements would need to be addressed with future tests and refinements (see section 1.8 for additional information) before publication of results. For example, the vertical data plots at slightly higher resistivities than the horizontal (by 0.03 Ω/m). If some natural grain orienting anisotropy developed as the sample settled prior to loading, the vertical resistivities should be slightly lower than the horizontal resistivities. The offset is small, but present in both kaolinite and quartz; thus, it should be monitored for future trials.

The vertical resistivities in both samples trend near exponentially after a short period of loading and are significantly higher than the horizontal data as porosity decreases. Resistivity is expected to generally increase, however, for quartz especially the different relative sizes of the responses are more significant than expected. The evolution of the horizontal data is more muted for both kaolinite and quartz. The distinct difference between the horizontal and vertical data raises the question of if the horizontal data is too muted or the vertical too large. There is a possibility of an edge effect, as the horizontal electrodes are close to the chamber base. As compaction occurs, sediment (especially clays) can compact to small thicknesses and may have some abnormal orientation around the detectors. Verification of an edge effect could include moving the horizontal electrodes to the chamber walls and raising the electrodes up the sides of the cell to see if there are changes in the data (see figure 1.4).

Equipment enhancements would likely further improve the accuracy and precision of data. Replacement of electrodes from stainless steel to titanium or another corrosion-resistant material will be a future modification. Additionally, thicker insulated/shielded wiring would improve containment and prevent stray voltage. A more complex adjustment would be to create a built-in waterproof housing for the wiring above the Teflon piston, where the detector connects to the circuit. We used silicon sealant and a water-resistant tape to prevent short-circuiting; however, a waterproof housing or maybe a small trench on the outside of the piston could prevent any small leakages present from impacting the electrode.

The most significant issues/errors we encountered are relatively easily addressed. As these were initial trials for a new prototype, some more efficient and precise equipment were not utilized due to accessibility and cost. Future additions such as a commercial impedance scanner, which can automatically account for the frequency/phase effects introduced by sample and electrode capacitances, would be a valuable addition.

An electrical impedance scanner would greatly reduce measurement error, subsequent calibrations, and the time intensiveness of manually taking readings. It would also allow for generally more accurate measurements when resistances fall between the whole numbers that the substitution boxes allow. The Wien’s bridge does allow for resistance and capacitance to be determined manually, however they are also automatically determined by certain commercial impedance scanners. With the high cost of these devices, they were not employed in this study. However, the Wien’s bridge system discussed here did allow for the initial validity test of this project to proceed. The results of this study are promising; thus the acquisition of a commercial impedance scanner will be pursued in the future. This would be a major improvement and necessary for publication quality data.

1.10 Conclusion

The scatter in the sample data has significantly decreased over time. This is visible when comparing the earlier kaolinite data to the later quartz data. The decreased data scatter is indicative that the apparatus and experimental construction have improved through the trials. The difference is also distinctly visible between very early trials not discussed here due to their limited longevity (issues of short-circuiting, stray voltage effects, etc…).

The prototype consolidometer has proven to effective in containing and measuring the sample, however improvements on other parts of the construction are important to continue this method development. (see section 1.9) This method shows promise for examining clay anisotropy and for future multifaceted experiments that can include concurrent seawater composition and salinity experiments. It is essential to collect comparative data on the same and similar sample types to determine the legitimacy of the trends observed here. However, the data stability and consistency have increased in each experiment conducted with this apparatus, which shows promise.

CHAPTER 2

Westerly granite gouge shearing trials: a collection of stick-slip data

2.0 Abstract

Fault healing and the seismic response following a slip period are integral in the evolution of fault systems. Fault healing and strengthening are dependent on factors including time, lithology, fluid content, velocity, and temperature. Dieterich 1972 found that the level of static friction is correlated to the logarithm time(Dieterich, 1972). This finding has become widely accepted for many materials and stays relatively consistent with additional factors such as fluid content and temperature. We collected and report here a large dataset of ~270 stick-hold-slip experiments that will be processed and built upon in the future.

2.1 Introduction

Brown et al. 2012 found that clay and fluid-rich environments can act as a lubricant in fault zones; however, the impact of this is very much dependent on the composition of the rock interface (Brown and Fialko, 2012). Hydrated clay minerals such as smectite have been shown to significantly enhance the likelihood of slip and the speed of slip(Oohashi et al., 2015). Velocity effects and slip rates are determining factors in the evolution of fault systems. Additionally, it has been found recently that higher velocity movements can lead to coseismic heating. Coseismic heating effects have been found to be a contributing factor in fault zone movement, especially in regard to high slip rate areas.

The overarching goal of this experiment was to advance the long-term project of Dr. Brown and others surrounding stick-slip friction experiments(Mitchell et al., 2011, 2015, 2016; Brown and Fialko, 2012). This would have been done by coupling composition and temperature changes to understand better how lithology will impact stick-slip events under varied hold times and temperature conditions. For the purposes of this study, the measurements were taken at 1mm/min and 5 mm/min. We did not include composition or temperature changes in these experiments due to time and lab accessibility constraints, however, they will be incorporated in the future.

The intentions of this study were to accomplish three things:

(1) Better understand the time dependence of frictional healing on pure Westerly Granite gouge.

(2) Create a base of time-dependent, slow rate friction trials to compare to in future studies

(3) Incorporate clay minerals like smectite and kaolinite to better match fault zone compositions.

2.2 Experimental setup

Westerly granite was chosen to build upon the work of Dr. Brown and past students/collaborators, and be able to use the studies from these prior tests for comparison(Mitchell et al., 2011, 2011, 2015; Brown and Fialko, 2012). The Westerly Granite sample was prepared by breaking down pieces of ‘standard’ westerly granite into a gouge size. Westerly granite has a composition of approximately 38% plagioclase feldspar, 29% quartz, 26% alkali feldspar, 3.8% biotite, 1.4% muscovite, and 0.8% chlorite(Rutter and Neumann, 1995). Once samples were sufficiently ground, they were integrated into the shear apparatus.

There are two pieces in the sample vessel of the direct shear apparatus. The bottom sample holder slots into part of the frame thus are held stable. The bottom vessel has 14.2 cm x 2.5 cm of exposed sample. The top and bottom pieces of the sample vessel are loaded with the sample prior to assembly (see section1.2, experimental methods). The top sample holder is shorter, with an exposed surface area of 10.5 cm x 2.6cm. This piece is situated as far from the stepper motor as possible while still having the top (smaller) sample area be in full contact with the bottom (longer) chamber. This allows for the maximum amount of space for consecutive hold-slip-hold trials. A containing plate is placed over the top chamber, providing a latching point for the stepper motor to provide horizontal movement (see figure 2.1).

The top sample holder is placed in direct contact with the hydraulic uniaxial compression system providing direct pressure (see figure 2.1) and attached to the stepper motor by a containing plate for the shearing movement.

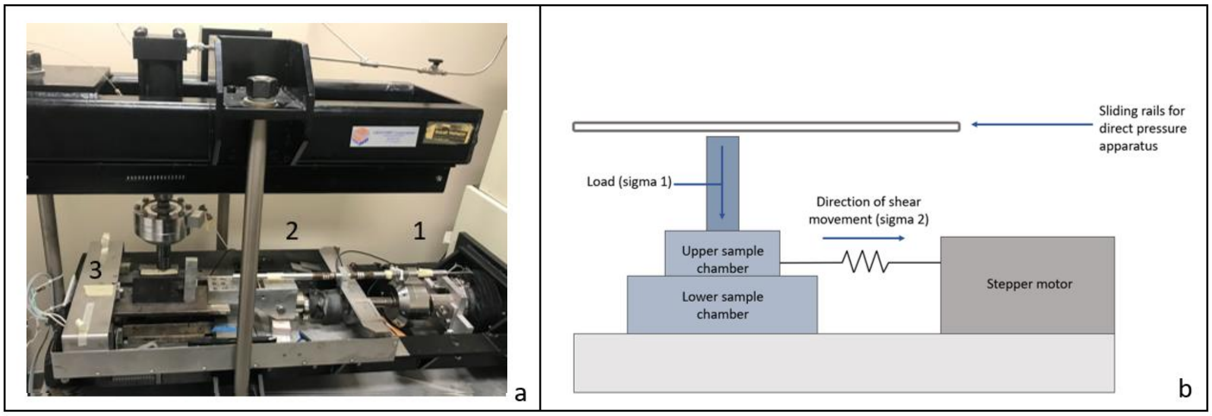

Figure 2.1: (a)Photo of experimental set up, with LVDT sensor numbers labeled. (b) General schematic of experimental set up

The Shear Large program runs the stepper motor, and controls the velocity, start, and stop initiations, and other movements related to re-setting the apparatus. An ISCO Series D pump controller is used to adjust the load of the hydraulic piston onto the sample. Three detectors are placed around the sample chamber to record stick-slip events, and the progression of the sliding experiment. The detectors and load evolution is recorded via the instrunet program, which is later exported for data analysis.

The LVDT detectors discussed here were produced by RDP Electronics(Type-LDC2000A, Serial-34620) and are accurate to ±0.05mm. The three detectors were calibrated against one another to ensure precision in the readings. The pressure pump, and ISCO Series D Model 500D syringe pump, self-calibrates and is rated to 0.15Mpa accuracy.

2.3 Experimental methods

As stated in section 2.1, the sample is repacked frequently as the gouge zone evolves, and small particles escape the sample chamber. Both top and bottom sample chambers are removed and cleaned during the re-setting process. The sample chambers are brushed to remove large particles and then wiped with a wet towel to remove the remaining particles and any small metal particles that were eroded off in the shearing process. The chambers are left to dry and then repacked with gouge. The gouge is manually compacted with a hammer and steel rectangles that fit into the chamber to evenly compress the sample. The sample is then dampened to aid in the consolidation process and compacted again. The sample chambers were then left to dry thoroughly overnight.

Intense compaction is not essential in the assembly process, as the first two shearing lengths re-evolve the gouge contact and will further compact the sample. The main purpose of this compaction process is to pack a sufficient amount of sample in the vessels and avoid the sample from escaping and affecting the steel-steel boundary slip when assembling the chambers. Within the 14.2 cm available distance for sliding runs, approximately 10-20 hold-slip-hold tests can be conducted, depending on the shearing speed. The same sample can be used repeatedly by re-setting the system, by moving the sample in reverse horizontally away from the stepper motor and releasing some of the pressure. With the very fine gouge grain-sized produced at this the boundary of the two sliding chambers, some particles eventually slip between the metal chambers causing abnormalities that are clear in the data and audibly heard. Once this starts to occur, the sample is removed and re-packed, the apparatus cleaned of any particles outside the sample chambers, and the last two movements across the length of the sample chamber are discarded to reduce error. Similarly, the beginning two full-length movements across the chamber are discarded, as the gouge material/fabric at the boundary between chambers takes at minimum one full length of movement to re-evolve. The gouge interface is visually very clear and can be seen in Figure 2.3.

2.4 Results

Approximately 270 stick-hold trials were conducted at speeds of 5mm/min and 1mm/min. Presented here is a graph showing the general distribution of hold times conducted. A 15 second standard was implemented early in the data collection as a way to calibrate the data in the future. The step motor is manually controlled, thus the timing was conducted on a secondary device. With that said, the precise hold time for the 15 second standards can be determined through data analysis. The specific hold times of longer experiments can not be determined in this way, as the data files become too big to work with if the entire hold-slip process is recorded. A 2 minute standard was implemented later in the data collection process to provide a secondary source of calibration.

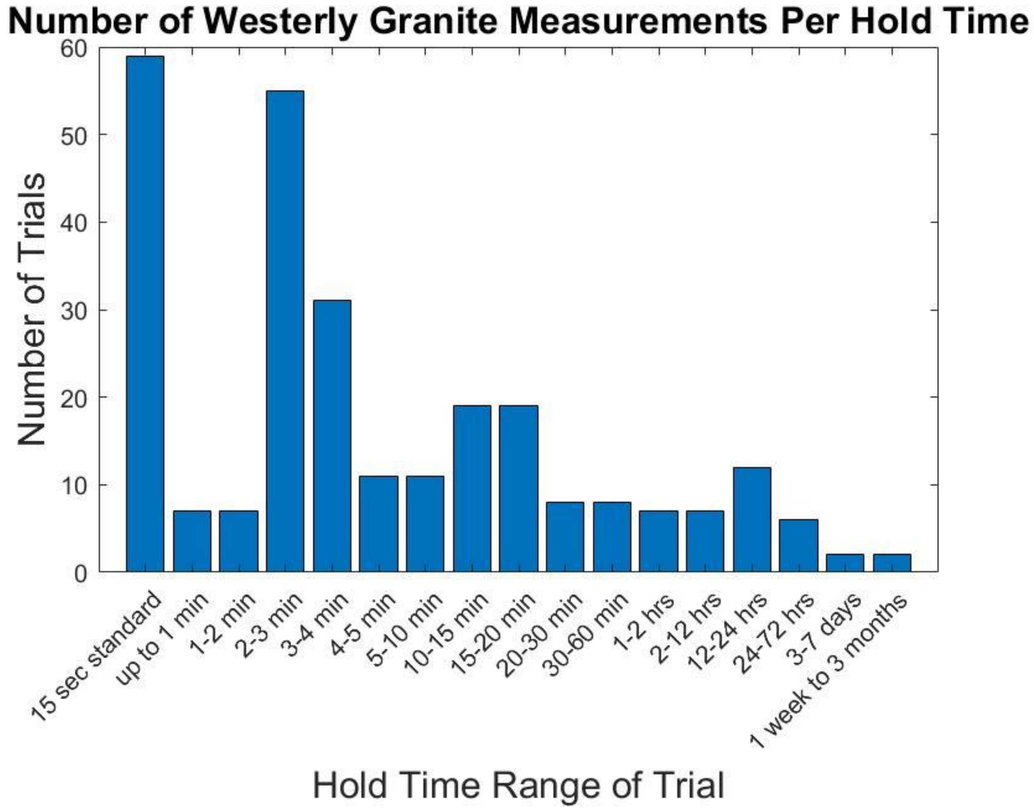

Figure 2.2: Bar chart comparing the number of trials collected to the hold time range.

Figure 2.3 shows the comparison of an unaltered sample of Westerly granite to an evolved gouge section after multiple stick-slip experiments.

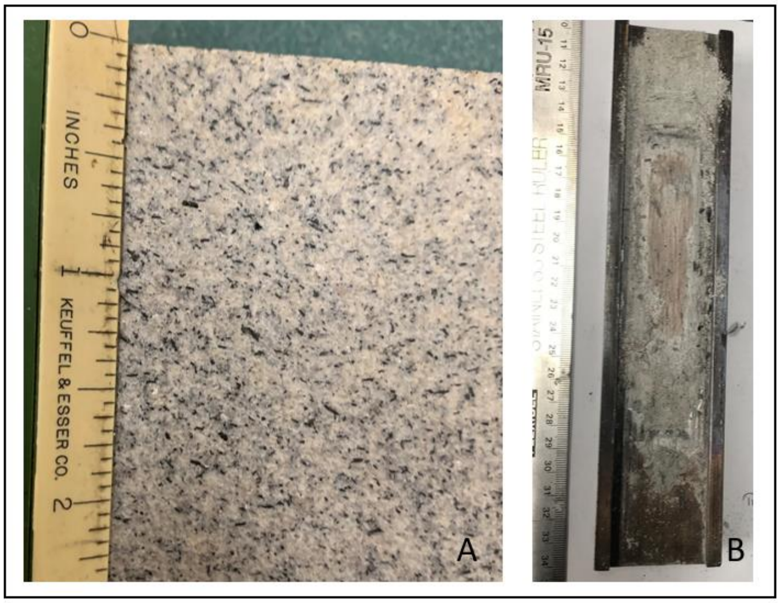

Figure 2.3: (A) Raw Westerly granite. (B) Evolved gouge contact after multiple stick-hold experiments.

2.5 Conclusion

With extenuating circumstances, a proper evaluation of the data for time dependence, and incorporation of clay minerals was not feasible. However, a collection of around 270 stick-slip responses were recorded with time as the (isolated) variable. Tests were conducted at 5 seconds to multi-month hold times. This provides a large base of data points to build on and compare with in the future when the new variables of temperature and composition changes are incorporated. A majority of this dataset is included with the submission of this thesis, instructions for understanding the raw files are included.

Appendix A

Resistivity - Archie's Law and Dual Water

Archie's law is a simplified expression of the relationship between porosity and resistivity, with the assumption that the silicate materials are essentially nonconductive, and the pore water has a conductivity or resistivity dependent on its salinity and temperature. Clean sands have small surface areas (<1 m^2/g) and fall close to a standard Archie type material such that:

$$F = \frac{C_w}{C_o} = \frac{R_t}{R_w} = \frac{b}{\phi^m} \qquad (1)$$

$$R_t = \tau_c \; R_w \, \phi^{-m} \, S^{-n} \qquad (2)$$

Where *F* is the formation factor, C_0-formation conductivity, R_t- formation resistivity, C_w- bulk pore water conductivity, R_w- bulk pore water resistivity, ϕ - fractional porosity, *m* - porosity coefficient lying between 1.8 and 2.0 for consolidated/cemented sands and closer to 1.3 for poorly consolidated sands, *b* – a formation constant, τ_c - the tortuosity, and *S* is the water saturation (equal to 1.0 in a water-saturated formation) with its coefficient *n*. Equation 1 should hold for most porosities above a critical value in clean sands as the surface area and conductive EDL volume are small, and the bulk pore water dominates. The *m* exponent starts to change as sand cements and porosities reduce, presumably as very small pores with conductive EDL effects become more prominent, and cements may have higher surface area minerals in them. Anisotropy in the tortuosity term, τ_c, becomes significant in clays due to their layered fabrics (see below) and for oriented fractures.

The basic Archie expression (equation 1) requires considerable modification for phyllosilicate containing sediments because (1) they have large negatively charged surface areas, (2) their attached exchange cations and thin EDL films are conductive, (3) bulk pore and EDL films can change average salinity and thin-film resistivity during consolidation, and (4) they are tabular minerals that form increasingly anisotropic structural mineral alignment and associate electrical fabrics during consolidation.

The Waxman-Smits Model is one of several that accounts for the presence of dual water in clay-containing sediments. Clay-containing sediments are known to be less electrically resistive (more conductive) than clean sands for a given porosity because their large surface areas allow for correspondingly volumetrically significant surrounding conductive EDL layers. We refer here to the basic “Dual Water “model that has been put forward in the oil industry to account for the electrical properties of hydrated clays during consolidation. There are several slightly different published versions of the Waxman-Smits equation. We refer you to equation 3 and the following reference for a further description of the equation and modifications (Freedman and Ausburn, 1985).

$$S_w^{n*} + R_W\, B\, Q_V\, S_w^{n*-1} - \frac{\varphi^{-m*}\, R_w}{R_t} = 0 \qquad (3)$$

Definitions of the variables are as follows :S_W - fractional water saturation, φ - fractional porosity, R_W- formation water resistivity (Ω m), R_T -formation resistivity (Ω m),

Q_V- the cation exchange capacity (meq/ml^{-1}), B –clay counterion conductance (mho m^{-1} ml – meq^{-1}). The superscripts n* and m* refer to the shaly sand saturation and cementation component, respectively.

All versions of the equation account for the additional conductivity imparted by the EDL and include a Cation Exchange Capacity (C_{ec} or Q_v in equations 3 and 4) term to account for the EDL effect. Essentially, in the "Dual Water" model the conductive EDL (mono film) layer and bulk pore water are given different electrical properties such that:

$$F^* = \frac{C_w + C_e}{C_0} = \frac{C_w + BQ_v}{C_0} = \frac{R_o}{R_w + R_e} \qquad (4)$$

where F^* is the clay formation factor, C_0– formation conductivity, C_w – bulk pore water, C_e - elevated EDL conductivity resulting from the clay exchange ions ($C_w < C_e$), B - ionic equivalent conductance of the exchange cations, Q_v - concentration of exchange cations (C_{ec}) per unit volume, and R_e is the resistance of the exchange cation layer ($R_w > R_e$). Clearly, as the bulk pore water is expelled we expect the resistivity of the fluids to become dominated by the EDL layer corresponding to Q_v as the bulk porosity falls and C_w is reduced.

Chapter 1 and 2 are coauthored with Brown, Kevin. The thesis author was the primary author of these chapters.

References

Abderrahmene, M., AbdelIllah, B., and Fouad, G., 2017, Electrical prediction of tortuosity in porous media: Energy Procedia, v. 139, p. 718–724, doi:10.1016/j.egypro.2017.11.277.

Brown, K.M., Poeppe, D., Josh, M., Sample, J., Even, E., Saffer, E., Tobin, H., Hirose, T., Kulongoski, J.T., Toczko, S., Maeda, L., and the IODP Expedition 348 Shipboard Party, 2017, The action of water films at Å-scales in the Earth: Implications for the Nankai subduction system: Earth and Planetary Science Letters, v. 463, p. 266–276, doi:10.1016/j.epsl.2016.12.042.

Brown, K., and Fialko, Y., 2012, “Melt welt” mechanism of extreme weakening of gabbro at seismic slip rates: Nature, v. 488, p. 638–41, doi:10.1038/nature11370.

Brown, K.M., and Ransom, B., 1996, Porosity corrections for smectite-rich sediments: Impact on studies of compaction, fluid generation, and tectonic history: Geology, v. 24, p. 843–846, doi:10.1130/0091-7613(1996)024<0843:PCFSRS>2.3.CO;2.

Brown, K.M., Saffer, D.M., and Bekins, B.A., 2001, Smectite diagenesis, pore-water freshening, and fluid flow at the toe of the Nankai wedge: Earth and Planetary Science Letters, v. 194, p. 97–109, doi:10.1016/S0012-821X(01)00546-5.

Butt, H.-J., Graf, K., and Kappl, M. Physics and Chemistry of Interfaces: , p. 376.

Diao, Y., and Espinosa-Marzal, R.M., 2018, The role of water in fault lubrication: Nature Communications, v. 9, p. 2309, doi:10.1038/s41467-018-04782-9.

Favaro, M., Jeong, B., Ross, P.N., Yano, J., Hussain, Z., Liu, Z., and Crumlin, E.J., 2016, Unravelling the electrochemical double layer by direct probing of the solid/liquid interface: Nature Communications, v. 7, p. 12695, doi:10.1038/ncomms12695.

Fitts, T.G., and Brown, K.M., 1999, Stress-induced smectite dehydration: ramifications for patterns of freshening and fluid expulsion in the N. Barbados accretionary wedge: Earth and Planetary Science Letters, v. 172, p. 179–197, doi:10.1016/S0012-821X(99)00168-5.

Freedman, R., and Ausburn, B., 1985, WAXMAN-SMITS EQUATION FOR SHALY SANDS: I. SIMPLE METHODS OF SOLUTION; II. ERROR ANALYSIS.: v. 26, p. 11–24.

Guo, Y., (Bill) Yu, X., and Department of Civil Engineering, Case Western Reserve University, 2104 Adelbert Road, Cleveland, OH 44106, USA, 2017, Characterizing the surface charge of clay minerals with Atomic Force Microscope (AFM): AIMS Materials Science, v. 4, p. 582–593, doi:10.3934/matersci.2017.3.582.

Holmboe, M., and Bourg, I.C., 2014, Molecular Dynamics Simulations of Water and Sodium Diffusion in Smectite Interlayer Nanopores as a Function of Pore Size and

Temperature: The Journal of Physical Chemistry C, v. 118, p. 1001–1013, doi:10.1021/jp408884g.

Kaufhold, S., Dohrmann, R., Stucki, J.W., and Anastácio, A.S., 2011, Layer Charge Density of Smectites – Closing the Gap Between The Structural Formula Method and the Alkyl Ammonium Method: Clays and Clay Minerals, v. 59, p. 200–211, doi:10.1346/CCMN.2011.0590208.

Mitchell, E., Fialko, Y., and Brown, K., 2015, Frictional properties of gabbro at conditions corresponding to slow slip events in subduction zones: Geochemistry, Geophysics, Geosystems, v. 16, p. n/a-n/a, doi:10.1002/2015GC006093.

Mitchell, E., Fialko, Y., and Brown, K., 2011, Temperature dependence of frictional healing of Westerly granite: Experimental observations and numerical simulations: AGU Fall Meeting Abstracts, v. 14, p. 2465, doi:10.1029/2012GC004241.

Mitchell, E., Fialko, Y., and Brown, K., 2016, Velocity-weakening behavior of Westerly granite at temperature up to 600 °C: FRICTIONAL PROPERTIES OF GRANITE: Journal of Geophysical Research: Solid Earth, doi:10.1002/2016JB013081.

Moore, J.C., and Saffer, D., 2001, Updip limit of the seismogenic zone beneath the accretionary prism of southwest Japan: An effect of diagenetic to low-grade metamorphic processes and increasing effective stress: Geology, v. 29, p. 183–186, doi:10.1130/0091-7613(2001)029<0183:ULOTSZ>2.0.CO;2.

Neuzil, C.E., and Provost, A.M., 2009, Recent experimental data may point to a greater role for osmotic pressures in the subsurface: Water Resources Research, v. 45, doi:https://doi.org/10.1029/2007WR006450.

Oohashi, K., Hirose, T., Takahashi, M., and Tanikawa, W., 2015, Dynamic weakening of smectite-bearing faults at intermediate velocities: Implications for subduction zone earthquakes: Journal of Geophysical Research: Solid Earth, v. 120, p. 1572–1586, doi:10.1002/2015JB011881.

Park, S.-J., and Seo, M.-K., 2011, Chapter 1 - Intermolecular Force, *in* Park, S.-J. and Seo, M.-K. eds., Interface Science and Technology, Elsevier, Interface Science and Composites, v. 18, p. 1–57, doi:10.1016/B978-0-12-375049-5.00001-3.

Poeppe, D.J., 2016, Permeability, Salinity, and Nanoscale Processes in Low Porosity Clay-Rich Sediments: UC San Diego, https://escholarship.org/uc/item/8q73h7jd (accessed May 2021).

Rutter, E.H., and Neumann, D.H.K., 1995, Experimental deformation of partially molten Westerly granite under fluid-absent conditions, with implications for the extraction of granitic magmas: Journal of Geophysical Research: Solid Earth, v. 100, p. 15697–15715, doi:10.1029/94JB03388.

Saffer, D.M., and Bekins, B.A., 2006, An evaluation of factors influencing pore pressure in accretionary complexes: Implications for taper angle and wedge mechanics: Journal of Geophysical Research: Solid Earth, v. 111, doi:10.1029/2005JB003990.

Saffer, D.M., and Wallace, L.M., 2015, The frictional, hydrologic, metamorphic and thermal habitat of shallow slow earthquakes: Nature Geoscience, v. 8, p. 594–600, doi:10.1038/ngeo2490.

Sayles, F.L., and Manheim, F.T., 1975, Interstitial solutions and diagenesis in deeply buried marine sediments: results from the Deep Sea Drilling Project: Geochimica et Cosmochimica Acta, v. 39, p. 103–127, doi:10.1016/0016-7037(75)90165-9.

Schleicher, A., Boles, A., and Van der Pluijm, B., 2015, Response of natural smectite to seismogenic heating and potential implications for the 2011 Tohoku earthquake in the Japan Trench: Geology, v. 43, p. 755–758, doi:10.1130/G36846.1.

Twiss, R.J., and Moores, E.M., 2006, Structural Geology: W. H. Freeman, 532 p.

Underwood, M.B., and Kubo, Y., 2013, Data Report: clay mineral assemblages in the Shikoku Basin, NanoTroSEIZE subduction inputs, IODP Sites C0011 and C0012: Integrated Ocean Drilling Program, Proceedings of the IODP 322, doi:10.2204/iodp.proc.322.2010.